Measurements of electric quadrupole transition frequencies in ^{226}Ra$^+$

C. A. Holliman,* M. Fan ◉, and A. M. Jayich ◉

Department of Physics, University of California, Santa Barbara, Santa Barbara, California 93106, USA
and California Institute for Quantum Entanglement, Santa Barbara, California 93106, USA

We report the first driving of the $7s\,^2S_{1/2} \rightarrow 6d\,^2D_{3/2}$ and $7s\,^2S_{1/2} \rightarrow 6d\,^2D_{5/2}$ electric quadrupole (E2) transitions in Ra$^+$. We measure the frequencies of both E2 transitions and two other low-lying transitions in ^{226}Ra$^+$ that are important for controlling the radium ion's motional and internal states: $6d\,^2D_{3/2} \rightarrow 7p\,^2P_{3/2}^o$ and $6d\,^2D_{5/2} \rightarrow 7p\,^2P_{3/2}^o$.

I. INTRODUCTION

The radium ion has two subhertz-linewidth electric quadrupole (E2) transitions from the ground state: $7s\,^2S_{1/2} \rightarrow 6d\,^2D_{5/2}$ at 728 nm and $7s\,^2S_{1/2} \rightarrow 6d\,^2D_{3/2}$ at 828 nm. The E2 transition to the $D_{5/2}$ state, which has a lifetime of ~300 ms [1], is useful for electron shelving, ground-state cooling, and controlling an optical qubit, and it could also serve as the clock transition for an optical clock [2]. Measuring these two quadrupole transitions across a chain of isotopes can be used to obtain information related to the nuclear structure of the radium isotopes, such as the specific mass shift and the change in mean-square nuclear charge radii [3,4]. The degree of nonlinearity in a King plot comparison of the two transitions could set bounds on new physics beyond the standard model [5]. There are 11 radium isotopes between mass number 213 and mass number 234 with half-lives longer than 1 min that could be ionized, trapped, and compared with a high precision on a King plot. A precision King plot can also be made using one E2 transition in Ra$^+$ and the Ra $^1S_0 \rightarrow^3 P_0$ intercombination line at 765 nm, which has a $2\pi \times 5$ mHz linewidth [6].

In this work we measure the two $7s \rightarrow 6d$ electric quadrupole transition frequencies, as well as the frequencies of the $6d\,^2D_{3/2} \rightarrow 7p\,^2P_{3/2}^o$ (708-nm) and $6d\,^2D_{5/2} \rightarrow 7p\,^2P_{3/2}^o$ (802-nm) electric dipole transitions (see Fig. 1) in ^{226}Ra$^+$ ($I = 0$, 1600-yr half-life). Previously the only optical frequency measurement in ^{226}Ra$^+$ with an uncertainty of less than 4 GHz is that of the $7s\,^2S_{1/2} \rightarrow 7p\,^2P_{1/2}^o$ (468-nm) Doppler cooling transition [7]. Combining that measurement with the measurements in this work, we calculate the $6d\,^2D_{3/2} \rightarrow 7p\,^2P_{1/2}^o$ (1079-nm) and $7s\,^2S_{1/2} \rightarrow 7p\,^2P_{3/2}^o$ (382-nm) frequencies, which are useful for laser-cooling Ra$^+$.

For our measurements we use a single laser-cooled radium ion, which is loaded by ablating a 10 μCi RaCl$_2$ target ~15 mm from the trap. The rf trapping voltage is turned on 20 μs after ablation to enhance loading efficiency. The radium ion trap and loading procedure used in this work were

described previously [7]. We use a heated iodine vapor cell as a frequency reference. The Ra$^+$ spectroscopy transitions and the iodine reference are driven with a tunable Ti:sapphire laser, whose frequency is recorded with a wavemeter (High Finesse WS-8) to determine the Ra$^+$ transition frequencies from the known iodine reference lines. We describe the Ra$^+$ transition measurements and fits in Sec. II and the iodine frequency reference spectroscopy in Sec. III. From the combined iodine and Ra$^+$ data we determine the Ra$^+$ transition frequencies in Sec. IV, and with these values we present an updated King plot that includes radium-226 in Sec. V.

II. RADIUM SPECTROSCOPY

The Ra$^+$ transitions are measured using state detection, where the ion is bright if the population is in the cooling cycle and dark otherwise. Bright-state fluorescence photons at 468 nm are collected onto a photomultiplier tube and the counts are then time-tagged with respect to the measurement pulse sequences [8]. In 1 ms of state detection 35 photons are collected on average if the population is in the $S_{1/2}$ or $D_{3/2}$ "bright" state and 1.5 photons of background scattered light if the population is shelved in the $D_{5/2}$ "dark" state. We set the bright-state detection threshold to 12 counts.

All Ra$^+$ spectroscopy pulse sequences begin with 0.5 ms of laser cooling and an initial state detection (see SD1 in Fig. 2). If the state detection finds the ion in the dark state, then the data point is excluded because the ion is not properly initialized. All pulse sequences finish with a second state detection step and then optical pumping to remove any remaining population from the $D_{5/2}$ state. We give a detailed description of the $7s\,^2S_{1/2} \rightarrow 6d\,^2D_{5/2}$ electric quadrupole "clock" transition measurement. The other measurements are similar, with brief descriptions provided.

A. $7s\,^2S_{1/2} \rightarrow 6d\,^2D_{5/2}$ (728 nm)

The pulse sequence for the clock transition measurement is shown in Fig. 2. Before each measurement we Doppler-cool the ion for 0.5 ms. The initial state detection determines whether the ion is cooled and whether the population is in a bright state (SD1). Any population in the $D_{3/2}$ state is then

---

*Corresponding author: cholliman3@gmail.com
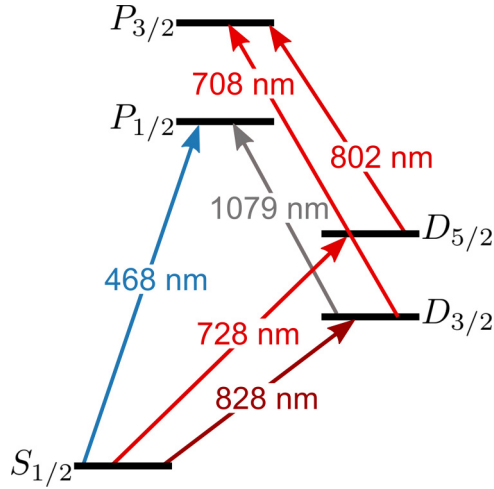
FIG. 1. The Ra$^+$ energy level structure showing the transitions driven in this work.

optically pumped with light at 1079 nm to the ground state (P1). The $7s\,^2S_{1/2} \to 6d\,^2D_{5/2}$ spectroscopy transition is then driven with light at 728 nm for 1 ms (P2), and if the light is on resonance, the population can be shelved to the $D_{5/2}$ state, and the shelving probability is measured with a second state detection (SD2). To prepare for the next measurement any shelved population is cleaned out with light at 802 nm, which drives the population to the $S_{1/2}$ and $D_{3/2}$ bright states (P3). Over many pulse sequences the 728-nm laser is swept over $\sim$100 MHz to drive all possible transitions between Zeeman levels of the two states. The $7s\,^2S_{1/2} \to 6d\,^2D_{5/2}$ spectroscopy is shown in Fig. 3, along with an inset of the corresponding iodine absorption reference spectrum.

To resolve the $S_{1/2} \to D_{5/2}$ and $S_{1/2} \to D_{3/2}$ Zeeman substructure of the transitions, a 7.8-G magnetic field is applied parallel to the trap's radio-frequency rods, which we define as the z axis. The magnetic field spreads the $S_{1/2} \to D_{5/2}$ transitions across $\sim$60 MHz. The energy splitting due to the
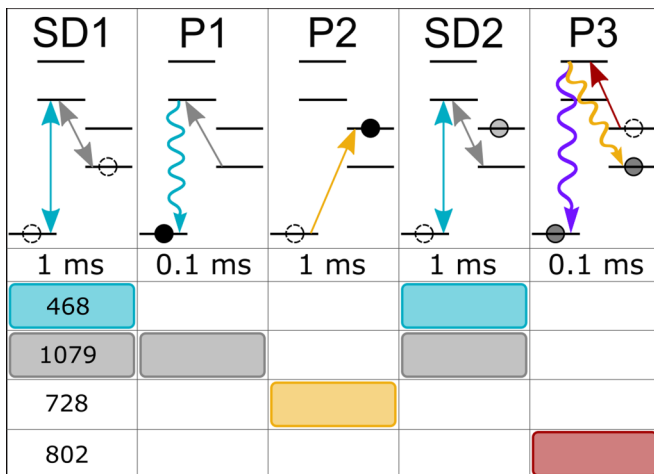

FIG. 2. The pulse sequence for the $^2S_{1/2} \to {}^2D_{5/2}$ E2 transition measurement. Squiggly lines depict E1 allowed decays, straight lines show optical pumping transitions, and double-arrows indicate optical cycling transitions.
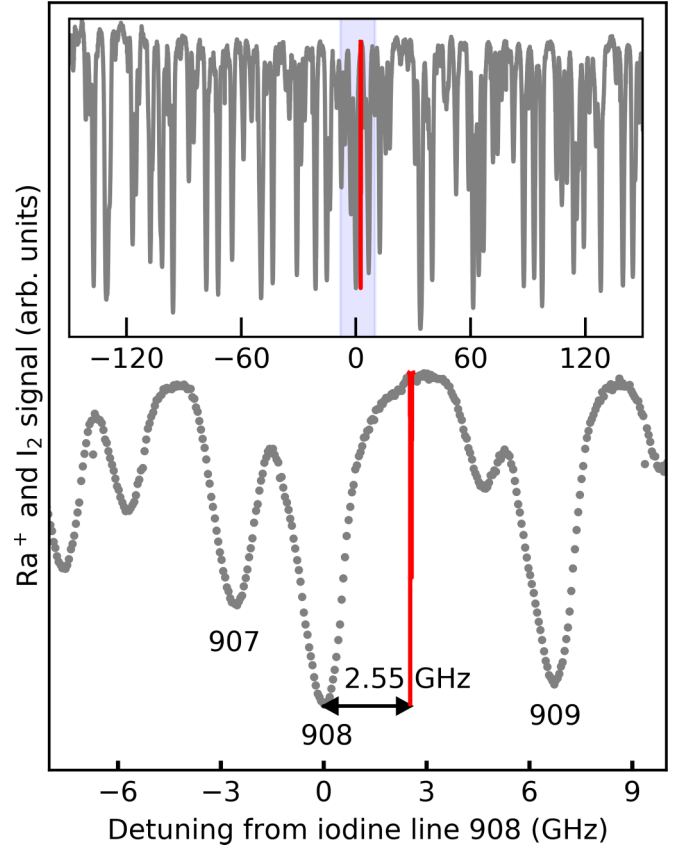

FIG. 3. The iodine absorption spectrum is plotted with the Ra$^+$ scan, where the iodine data (gray) and Ra$^+$ data (red; see Fig. 4) are scaled and offset to highlight the detuning between the transitions. We use the line indices from [9] to denote iodine lines. Inset: Iodine lines in a 300-GHz range around the closest reference line, 908, with the outset region highlighted in blue.

applied magnetic field is calculated from $\Delta E_j = g_j \mu_B B m$, where g_j is the Landé g-factor for state with total angular momentum j, m is the magnetic quantum number, B is the magnetic field. The Rabi frequency for transitions between the $S_{1/2,m}$ and $D_{5/2,m'}$ Zeeman levels is

$$\Omega = \left| \frac{eE_0}{2\hbar} \langle S_{1/2} || r^2 \mathbf{C}^{(2)} || D_{5/2} \rangle \right.$$

$$\left. \times \sum_{\Delta m=-2}^{2} \begin{pmatrix} 1/2 & 2 & 5/2 \\ -m & \Delta m & m' \end{pmatrix} g^{(\Delta m)} \right|, \quad (1)$$

where $\langle S_{1/2} || r^2 \mathbf{C}^{(2)} || D_{5/2} \rangle$ is the reduced matrix element, the summation is over Wigner 3-j symbols and a geometry-dependent factor, $g^{(\Delta m)}$ [10,11], given by

$$g^{(0)} = \frac{1}{2} |\cos(\gamma)\sin(2\phi)|,$$

$$g^{(\pm 1)} = \frac{1}{\sqrt{6}} |\cos(\gamma)\cos(2\phi) + i\sin(\gamma)\cos(\phi)|,$$

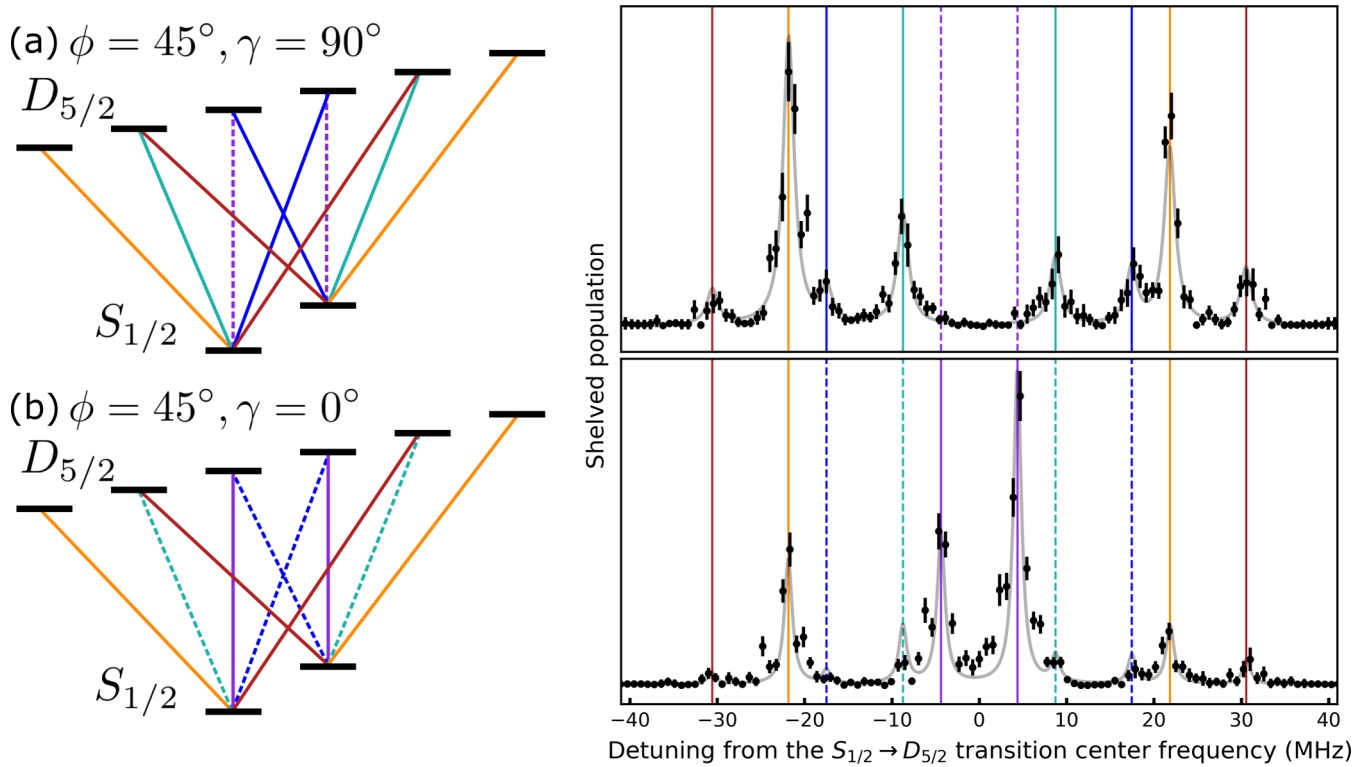$$g^{(\pm 2)} = \frac{1}{\sqrt{6}} \left| \frac{1}{2}\cos(\gamma)\sin(2\phi) + i\sin(\gamma)\sin(\phi) \right|, \quad (2)$$

FIG. 4. Two measurements of the $S_{1/2} \rightarrow D_{5/2}$ transition with angle $\phi = 45°$ between the k vector and the magnetic field: (a) angle $\gamma = 90°$ between the laser polarization and the magnetic field, which suppresses $\Delta m = 0$; (b) $\gamma = 0°$, which suppresses $\Delta m = \pm 1$. Dashed lines indicate transitions suppressed by the choice of ϕ and γ. Symmetric pairs of transitions are the same color. Error bars are the most likely 68% confidence interval of a binomial distribution.

where Δm is the change in the magnetic quantum number, ϕ is the angle between the laser's k vector and the magnetic field, and γ is the angle between the laser polarization and the magnetic field vector projected into the plane of incidence.

For E2 transitions $\Delta m = 0, \pm 1, \pm 2$ are allowed, which gives rise to 10 transitions between Zeeman levels for $S_{1/2} \rightarrow D_{5/2}$. We measure these transitions using $\phi = 45°$ and two values of γ, $0°$ and $90°$, which suppress certain $|\Delta m|$ transitions (see Fig. 4). We fit the spectroscopy data to a sum of 10 Lorentzians, from which we extract the applied magnetic field, ϕ, γ, and the $S_{1/2} \rightarrow D_{5/2}$ transition frequency. Due to the 468- and 1079-nm laser polarizations, during Doppler cooling the ground state $m = -1/2$ level is preferentially populated and so reduces the probability of transition occurring from the $m = 1/2$ level. The ground-state population imbalance is one of the fitting parameters. The $\sim$0.5-Hz natural linewidth of the $S_{1/2} \rightarrow D_{5/2}$ transition is broadened by laser power and magnetic field fluctuations. There are small micromotion sidebands in the spectrum at our trap drive frequency, 1.8 MHz. We average the two center frequencies extracted from the two fits of the spectra at different values of γ to determine the $S_{1/2} \rightarrow D_{5/2}$ transition frequency.

B. $6d\ ^2D_{5/2} \rightarrow 7p\ ^2P_{3/2}^o$ (802 nm)

For measuring both the $^2D_{5/2} \rightarrow ^2P_{3/2}$ and the $^2D_{3/2} \rightarrow ^2P_{3/2}$ transitions a magnetic field of $\sim$2.5 G is applied to prevent coherent dark states [12]. After initialization, the ion

is optically pumped to the $D_{5/2}$ state with light at 468 and 708 nm for 60 μs. Any population in the $D_{5/2}$ state is then pumped with the spectroscopy light at 802 nm for 150 μs. If the light is on resonance, the population can be driven to the $P_{3/2}$ state, where decays will populate the bright states (see Fig. 5). After the second state detection the $D_{5/2}$ state is optically pumped with resonant 802-nm light from an external cavity diode laser.

To determine the line center for the $D_{5/2} \rightarrow P_{3/2}$ transition we fit the data to a Lorentzian (see Fig. 5). The full
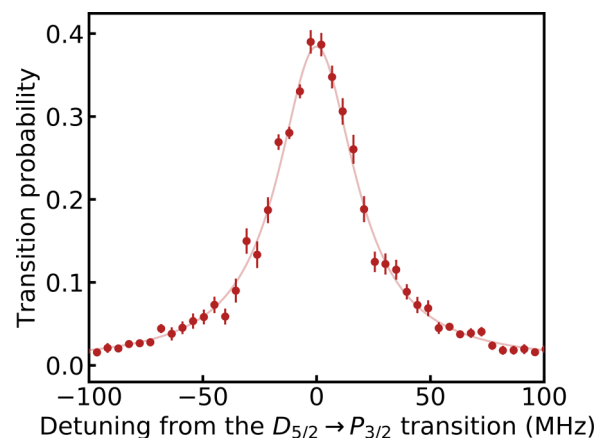

FIG. 5. Spectroscopy of the $D_{5/2} \rightarrow P_{3/2}$ transition. A Lorentzian fit gives an FWHM of 41.5(9) MHz.

width at half-maximum (FWHM) of 41.5(9) MHz gives a lower bound of 3.84(9) ns for the $P_{3/2}$-state lifetime, which agrees with the calculated value of 4.73 ns [1]. The 802-nm laser light is incident on the ion along the trap's z axis to minimize micromotion broadening [13]. We measured the 802-nm laser's beam waist to be 300(50) μm and our beam power to be 1.2(1) μW. We estimate that the transition is power broadened by ~8 MHz from the 802-nm beam waist and power.

C. $7s\,^2S_{1/2} \rightarrow 6d\,^2D_{3/2}$ (828 nm)

After initialization, any population in the $D_{3/2}$ state is optically pumped with light at 1079 nm for 100 μs to the ground state. The $7s\,^2S_{1/2} \rightarrow 6d\,^2D_{3/2}$ transition is driven with light at 828 nm for 10 ms, and if the light is on resonance, the ion can be shelved to the $D_{3/2}$ state. Any population in the $D_{3/2}$ state is then pumped with light at 708 nm for 60 μs, which drives the population to the $P_{3/2}$ state whose decays populate the $S_{1/2}$ and $D_{5/2}$ states.

The population is shelved to the $D_{5/2}$ state with a low fidelity due to the branching fraction from the $P_{3/2}$ state. The shelved probability is determined from a binomial distribution of k shelved events (corresponding to fewer than 12 photons collected during the second state detection) in n trials (where the ion is properly initialized at the beginning of the pulse sequence). There are eight transitions between Zeeman levels for the $S_{1/2} \rightarrow D_{3/2}$ transition. We fit the spectra in a similar fashion as the $S_{1/2} \rightarrow D_{5/2}$ transition to extract the center frequency.

D. $6d\,^2D_{3/2} \rightarrow 7p\,^2P_{3/2}^o$ (708 nm)

After initialization, any population in the $S_{1/2}$ state is optically pumped with light at 468 nm for 100 μs to the $D_{3/2}$ state. The population is then pumped with light at 708 nm for 50 μs, and if the light is on resonance, the population can be driven to the $P_{3/2}$ state whose decays populate the $S_{1/2}$ and $D_{5/2}$ bright states. The data are fit to a Lorentzian to determine the center frequency.

III. IODINE FREQUENCY REFERENCE

For iodine absorption spectroscopy the Ti:sapphire laser is scanned at 10 MHz per second across a frequency range that includes at least two iodine reference lines, as well as the target Ra$^+$ transition. To reduce drift in the wavemeter measurement we measure the iodine spectra both before and after Ra$^+$ spectroscopy. We use a single iodine line as the frequency reference, and determine the lines frequency by fitting the dip corresponding to the iodine line in both scans to a Voigt function and averaging the two centers. We then calibrate the iodine line frequency we measured with a wavemeter to an absolute frequency using IodineSpec5 [14,15], which provides a comprehensive I$_2$ reference data set based on iodine spectrum measurements including the original iodine atlas work [9]. We fit the corresponding absorption dip in the IodineSpec5 data set to a Voigt function to determine the absolute frequency of the measured iodine line center.

The ^{127}I$_2$ vapor cell frequency reference (75 mm long, with a 19-mm outer diameter and windows angled at 11°) is heated

in a tube furnace to ~500° C, the temperature at which the iodine atlas lines were measured [9]. We scan the temperature of the I$_2$ cell by ±50° C around 500° C and vary an applied magnetic field by ±4 G, and for both we find frequency shifts within the fitting uncertainty. To compensate for laser power drifts the power is recorded on a reference photodiode before the iodine cell.

IV. Ra TRANSITION FREQUENCIES

The Ra$^+$ transition frequencies are calculated from the frequency difference between the radium and the iodine reference line centers that are recorded with a wavemeter. The fit iodine reference lines calculated in IodineSpec5 are used to calibrate the wavemeter frequencies.

The closest iodine reference line to the $S_{1/2} \rightarrow D_{5/2}$ transition is line 908 from [9], which we calculate using IodineSpec5 to be 412 004.754(15) GHz. From the difference between radium and iodine spectroscopy center fits, 2.947 GHz, we determine a transition frequency of 412 007.701(18) GHz. We take the total uncertainty in our measurements to be $\sigma_{\text{total}} = \sqrt{\sigma_{\text{Ra}^+}^2 + \sigma_{\text{I}_2}^2 + \sigma_{\text{spec}}^2 + \sigma_{\text{wm}}^2}$, where σ_{Ra^+} is the radium fitting uncertainty, σ_{I_2} is the measured iodine fitting uncertainty, σ_{spec} is the IodineSpec5 line uncertainty, and σ_{wm} is the wavemeter uncertainty, 10 MHz. The IodineSpec5 line uncertainties range from 2 to 45 MHz for the lines referenced in this work. The IodineSpec5 fitting uncertainties are on the kilohertz level and are negligible compared to the other uncertainties.

The reported value for the $D_{3/2} \rightarrow P_{1/2}$ transition, 277 818.95(8) GHz, comes from the frequency difference between the $S_{1/2} \rightarrow D_{3/2}$ E2 transition measured in this work and the measurement of the $S_{1/2} \rightarrow P_{1/2}$ transition by Fan *et al.* [7].

From our measurements we can calculate the $S_{1/2} \rightarrow P_{3/2}$ (382-nm) transition frequency by summing either the 728- and 802-nm frequencies, 785 722.10(3) GHz, or the 828- and 708-nm frequencies, 785 722.07(5) GHz. Both pairs of transitions originate in the ground state and end in the $P_{3/2}$ state. The two calculated frequencies are in good agreement, and we report the value calculated from the 728- and 802-nm frequencies, as the uncertainty in the underlying measurements is smaller. The measured and calculated frequencies are summarized in Table I.

TABLE I. Summary of ^{226}Ra$^+$ frequency measurements. All units are GHz. *Frequencies calculated from measurements. † Frequencies extrapolated from a King plot [16].

Transition	[17]	[2]	This work [7]
$S_{1/2} \rightarrow P_{3/2}$	785 723(4)	785 721.670(70)*	785 722.10(3)*
$S_{1/2} \rightarrow P_{1/2}$	640 092(7)	640 096.647(23)*	640 096.63(6) [7]
$D_{3/2} \rightarrow P_{3/2}$	423 438(6)	⋯	423 444.39(3)
$S_{1/2} \rightarrow D_{5/2}$	⋯	⋯	412 007.701(18)
$D_{5/2} \rightarrow P_{3/2}$	373 717(5)	⋯	373 714.40(2)
$S_{1/2} \rightarrow D_{3/2}$	⋯	362 277.361(33)†	362 277.68(5)
$D_{3/2} \rightarrow P_{1/2}$	⋯	277 819.285(18)†	277 818.95(8)*

TABLE II. Measured Ra$^+$ isotope shifts of the 468-, 708-, and 1079-nm transitions for $^{210-213}$Ra$^+$ and ^{226}Ra$^+$ relative to ^{214}Ra$^+$. All units are MHz. The 468-nm isotope shifts are from [19]. The 708- and 1079-nm isotope shifts for $^{210-213}$Ra$^+$ are from [22]. *An isotope shift calculated in this work.

Isotope	468 nm	708 nm	1079 nm
210	8449(6)	⋯	−1884(16)
211	7770(4)	⋯	−1755(14)
212	4583(3)	−701(20)	−1025(12)
213	3049(3)	−453(34)	−707(14)
214	0	0	0
226	−57 852(18)	9403(27)*	13 294(76)*

There are discrepancies between the transition frequencies measured in this work and those reported by Nunez *et al.* [2] (see Table I). We are able to resolve some of the discrepancies by redoing the analysis in [2]. The $D_{3/2} \to P_{1/2}$ transition frequency reported in [2], 277 819.285(18) GHz, is extrapolated from a King plot with data from Giri *et al.* [16]. From the 1079 nm/482 nm King plot (Fig. 4 in [16]) we find a slope of −0.342(7) and a y intercept of −2.2(5) THz amu, which gives the transformed isotope shift [see Eq. (4) below] of 54.5(1.3) THz amu and the $D_{3/2} \to P_{1/2}$ transition frequency in ^{226}Ra$^+$ of 277 819.2(3) GHz. This value agrees with our measurement. The $S_{1/2} \to D_{3/2}$ transition frequency reported in [2] is calculated from the frequency difference between the $S_{1/2} \to P_{1/2}$ and the $D_{3/2} \to P_{1/2}$ transitions. With the recalculated value of the $D_{3/2} \to P_{1/2}$ frequency, the $S_{1/2} \to D_{3/2}$ transition frequency is 362 277.4(3) GHz, which is also in agreement with our measurement. There remains the discrepancy between the $S_{1/2} \to P_{3/2}$ frequency measured in this work and the value reported in [2]. This discrepancy could be resolved by direct spectroscopy of the $S_{1/2}$-to-$P_{3/2}$ transition in one of many radium isotopes, including isotope(s) 212, 214, or 221–226 [18].

V. KING PLOT

We determine isotope shifts for the 708- and 1079-nm transitions in ^{226}Ra$^+$. The isotope shift between a target and a reference isotope is $\delta\nu_{MM'} = \nu_M - \nu_{M'}$, where M is the target isotope nuclear mass, M' is the reference isotope nuclear mass, and ν is the transition frequency. We use ^{214}Ra$^+$, which has a closed neutron shell, as the reference isotope [19]. The 1079-nm ^{214}Ra$^+$ reference frequency is 277 805.656 GHz [16] and the 708-nm ^{214}Ra$^+$ reference frequency is 423 434.989 GHz [20]. Isotope shifts of 468, 708, and 1079 nm are listed in Table II. The isotope shift is

TABLE III. ^{226}Ra$^+$ field shift ratios.

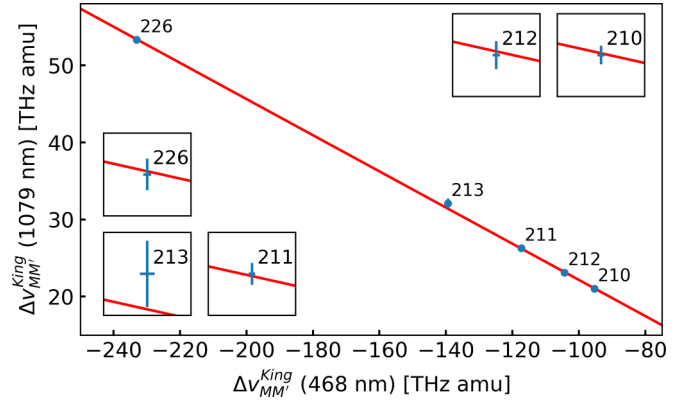| FS ratio	Theory [22]	Experiment [22]	This work
F_{708}/F_{468}	−0.16(1)	−0.136(57)	−0.171(3)
F_{1079}/F_{468}	−0.23(2)	−0.244(11)	−0.235(2)

FIG. 6. A King plot of the transformed isotope shifts of the $D_{3/2} \to P_{1/2}$ versus the $S_{1/2} \to P_{1/2}$ transitions. The reference isotope is ^{214}Ra$^+$. Insets: Magnifications of ×200 for the 468-nm axis and ×50 for the 1079-nm axis.

parameterized as

$$\delta\nu_{MM'} = (K_{\mathrm{NMS}} + K_{\mathrm{SMS}})\frac{M - M'}{MM'} + F_{\mathrm{FS}}\lambda_{MM'}, \qquad (3)$$

where K_{NMS} and K_{SMS} are the normal and specific mass shifts, F_{FS} is the field shift, and $\lambda_{MM'}$ is the Seltzer moment, which to lowest order is the difference in mean square nuclear charge radii, $\lambda_{MM'} \approx \delta\langle r^2\rangle_{MM'}$ [3]. The transformed isotope shift is

$$\Delta\nu_{MM'}^{\mathrm{King}} = \delta\nu_{MM'}\frac{MM'}{M - M'} - K_{\mathrm{NMS}}, \qquad (4)$$

from which the ratio of field shifts between transitions and the difference in specific mass shifts can be determined [21]. King plot comparisons of the transformed isotopes shifts give the Ra$^+$ field shift ratios, $F_{708}/F_{468} = -0.171(3)$ and $F_{1079}/F_{468} = -0.235(2)$, which are summarized in Table III. The 1079 nm/468 nm King plot is shown in Fig. 6.

VI. CONCLUSION

The first driving of the 728- and 828-nm electric quadrupole transitions in ^{226}Ra$^+$ lays the groundwork for quantum information science and precision measurement experiments with Ra$^+$. Isotope shift spectroscopy of Ra$^+$ dipole transitions has been done at the ISOLDE facility at CERN and could be extended to a high precision by trapping Ra$^+$ and measuring the E2 transitions [23]. Estimates for the nonlinearities of a King plot of radium's two narrow linewidth transitions following [24] could guide searches to constrain new physics.

[1] R. Pal, D. Jiang, M. S. Safronova, and U. I. Safronova, Phys. Rev. A **79**, 062505 (2009).

[2] M. Nuñez Portela, E. A. Dijck, A. Mohanty, H. Bekker, J. E. van den Berg, G. S. Giri, S. Hoekstra, C. J. G. Onderwater, S. Schlesser, R. G. E. Timmermans, O. O. Versolato, L. Willmann, H. W. Wilschut, and K. Jungmann, Appl. Phys. B **114**, 173 (2014).

[3] K. Heilig and A. Steudel, At. Data Nucl. Data Tables **14**, 613 (1974).

[4] P.-G. Reinhard, W. Nazarewicz, and R. F. Garcia Ruiz, arXiv:1911.00699.

[5] J. C. Berengut, D. Budker, C. Delaunay, V. V. Flambaum, C. Frugiuele, E. Fuchs, C. Grojean, R. Harnik, R. Ozeri, G. Perez, and Y. Soreq, Phys. Rev. Lett. **120**, 091801 (2018).

[6] J. Bieroń, P. Indelicato, and P. Jönsson, Eur. Phys. J. Spec. Topics **144**, 75 (2007).

[7] M. Fan, C. A. Holliman, A. L. Wang, and A. M. Jayich, Phys. Rev. Lett. **122**, 223001 (2019).

[8] T. Pruttivarasin and H. Katori, Rev. Sci. Instrum. **86**, 115106 (2015).

[9] S. Gerstenkorn, J. Verges, and J. Chevillard, *Atlas du spectre d'absorption de la molecule d'iode: 11000–14000 cm to the minus 1* (Laboratoire Aime-Cotton CNRS II, Paris, 1982); S. Gerstenkorn and P. Luc, *Atlas du spectre d'absorption de la molecule d'iode: 14000–15600 cm to the minus 1* (Laboratoire Aime-Cotton CNRS II, Paris, 1982).

[10] D. F. V. James, Appl. Phys. B **66**, 181 (1998).

[11] C. Roos, Ph.D. thesis, University of Innsbruck, 2000.

[12] D. J. Berkeland and M. G. Boshier, Phys. Rev. A **65**, 033413 (2002).

[13] D. J. Berkeland, J. D. Miller, J. C. Bergquist, W. M. Itano, and D. J. Wineland, J. Appl. Phys. **83**, 5025 (1998).

[14] H. Knöckel and E. Tiemann, *IodineSpec5* (Universität Hannover, Hannover, 2011).

[15] H. Knöckel, B. Bodermann, and E. Tiemann, Eur. Phys. J. D **28**, 199 (2004).

[16] G. S. Giri, O. O. Versolato, J. E. van den Berg, O. Böll, U. Dammalapati, D. J. van der Hoek, K. Jungmann, W. L. Kruithof, S. Müller, M. Nuñez Portela, C. J. G. Onderwater, B. Santra, R. G. E. Timmermans, L. W. Wansbeek, L. Willmann, and H. W. Wilschut, Phys. Rev. A **84**, 020503(R) (2011).

[17] E. Rasmussen, Z. Phys. **86**, 24 (1933).

[18] W. Neu, R. Neugart, E. W. Otten, G. Passler, K. Wendt, B. Fricke, E. Arnold, H. J. Kluge, and G. Ulm, Z. Phys. D **11**, 105 (1989).

[19] K. Wendt, S. A. Ahmad, W. Klempt, R. Neugart, E. W. Otten, and H. H. Stroke, Z. Phys. D **4**, 227 (1987).

[20] O. O. Versolato, G. S. Giri, L. W. Wansbeek, J. E. van den Berg, D. J. van der Hoek, K. Jungmann, W. L. Kruithof, C. J. G. Onderwater, B. K. Sahoo, B. Santra, P. D. Shidling, R. G. E. Timmermans, L. Willmann, and H. W. Wilschut, Phys. Rev. A **82**, 010501(R) (2010).

[21] W. H. King, J. Opt. Soc. Am. **53**, 638 (1963).

[22] L. W. Wansbeek, S. Schlesser, B. K. Sahoo, A. E. L. Dieperink, C. J. G. Onderwater, and R. G. E. Timmermans, Phys. Rev. C **86**, 015503 (2012).

[23] K. M. Lynch, S. G. Wilkins, J. Billowes, C. L. Binnersley, M. L. Bissell, K. Chrysalidis, T. E. Cocolios, T. D. Goodacre, R. P. de Groote, G. J. Farooq-Smith, D. V. Fedorov, V. N. Fedosseev, K. T. Flanagan, S. Franchoo, R. F. Garcia Ruiz, W. Gins, R. Heinke, i Koszorus, B. A. Marsh, P. L. Molkanov, P. Naubereit, G. Neyens, C. M. Ricketts, S. Rothe, C. Seiffert, M. D. Seliverstov, H. H. Stroke, D. Studer, A. R. Vernon, K. D. A. Wendt, and X. F. Yang, Phys. Rev. C **97**, 024309 (2018).

[24] V. V. Flambaum, A. J. Geddes, and A. V. Viatkina, Phys. Rev. A **97**, 032510 (2018).

Correction: A minor error in Eq. (1) has been corrected, and an entry typeset incorrectly in Table II has been fixed.